SCIENTIFIC REPORTS

OPEN

SUBJECT AREAS:
MATERIALS SCIENCE
LITHOGRAPHY

Received
3 April 2014

Accepted
21 May 2014

Published
16 June 2014

Correspondence and requests for materials should be addressed to X.S.M. (miaoxs@mail.hust.edu.cn)

Metallic resist for phase-change lithography

Bi Jian Zeng[1,2], Jun Zhu Huang[1,2], Ri Wen Ni[1,2], Nian Nian Yu[1,2], Wei Wei[1,2], Yang Zhi Hu[1,2], Zhen Li[1,2] & Xiang Shui Miao[1,2,3]

[1]Wuhan National Laboratory for Optoelectronics, Huazhong University of Science and Technology, LuoYu Road, Wuhan 430074, China, [2]School of Optical and Electronic Information, Huazhong University of Science and Technology, LuoYu Road, Wuhan 430074, China, [3]Wuhan National High Magnetic Field Center, Huazhong University of Science and Technology, Wuhan 430074, China.

Currently, the most widely used photoresists in optical lithography are organic-based resists. The major limitations of such resists include the photon accumulation severely affects the quality of photolithography patterns and the size of the pattern is constrained by the diffraction limit. Phase-change lithography, which uses semiconductor-based resists such as chalcogenide $Ge_2Sb_2Te_5$ films, was developed to overcome these limitations. Here, instead of chalcogenide, we propose a metallic resist composed of $Mg_{58}Cu_{29}Y_{13}$ alloy films, which exhibits a considerable difference in etching rate between amorphous and crystalline states. Furthermore, the heat distribution in $Mg_{58}Cu_{29}Y_{13}$ thin film is better and can be more easily controlled than that in $Ge_2Sb_2Te_5$ during exposure. We succeeded in fabricating both continuous and discrete patterns on $Mg_{58}Cu_{29}Y_{13}$ thin films via laser irradiation and wet etching. Our results demonstrate that a metallic resist of $Mg_{58}Cu_{29}Y_{13}$ is suitable for phase change lithography, and this type of resist has potential due to its outstanding characteristics.

Although sub-100-nm lithography resolution can be achieved using electron-beam lithography (EBL)[1], this technique is not optimal because of its extremely high cost and poor efficiency. In contrast, it is difficult to create sub-diffraction[2,3] nanopatterns using optical lithography because of the diffraction limit[4]. Although it is possible to improve the resolution by increasing the numeral aperture (N.A.) of the objective lens or decreasing the wavelength of the incident laser, "1" is the ideal maximum N.A. value possible in air, and 157 nm[5] is considered to be the shortest wavelength that can be achieved for current optical lithography in air. Moreover, the most widely used photoresists in optical lithography are organic-based resists, which may not only cause the borders of lithography patterns to blur but also present a health risk to users because of their toxicity. Semiconductor-based resists such as chalcogenide $Ge_2Sb_2Te_5$ have been used for phase-change lithography (PCL)[6–14], which is based on the etching-rate (solubility) difference between the amorphous (as-deposited) and crystalline (annealed) states of phase-change materials in acid/alkaline solution. Because the Gaussian profile of the laser beam intensity confines the "phase-change" process well within the localised laser-heated area, it would efficiently fabricate sub-diffraction structures[15,16] and femtosecond laser source[17–19] would be an appropriate option to achieve a fine feature size.

Metallic glasses, which exhibit excellent performance in terms of strength, elastic limit strain, corrosion resistance and abrasion resistance[20–27], have recently attracted the increasing attention of many researchers[28–31]. In general, metallic glasses are metals and are good heat conductors, so metallic glass has been applied as a thermal absorption layer[27] in phase-change lithography. In addition, metallic glasses also exhibit both "amorphous" and "crystalline" states, similar to chalcogenide-based phase-change materials. This feature indicates that metallic glasses may have the potential to be directly used as metallic resists. However, the use of metallic materials as etching layers in lithography has not yet been reported. In this report, we propose a metallic resist consisting of a thin film of $Mg_{58}Cu_{29}Y_{13}$ (MgCuY) alloy, which presents considerable etching selectivity between the crystalline and amorphous states. Unlike organic resists, this metallic resist is non-toxic. Moreover, the use of a metallic resist is expected to reduce production cost because abundant metal elements are readily available in nature. This is the first report to demonstrate the feasibility of a metallic resist using MgCuY alloy, and we expect that because of the outstanding characteristics of metal, "metallic resists" will surely play an important role in lithography in the future.

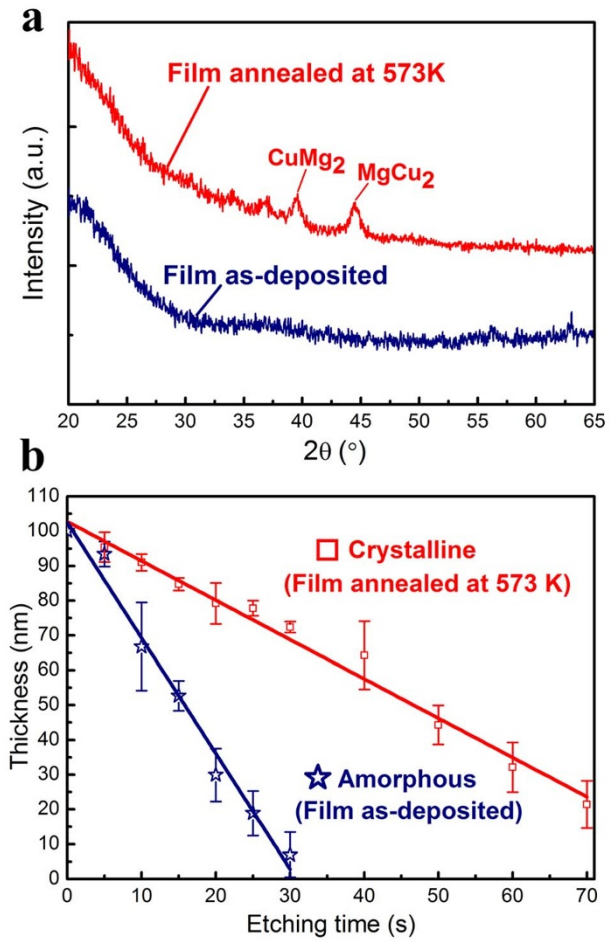

Figure 1 | Different etch rates for as-deposited and crystalline MgCuY thin films. (a) XRD patterns acquired from an as-deposited MgCuY thin film and from a film annealed at 573 K for 30 min. (b) Etching characteristics of a sputter-deposited MgCuY thin film in 0.5 wt% nitric acid/ethanol solution under magnetic stirring at 300 rpm. The initial thicknesses of the as-deposited (amorphous) and crystalline samples were both approximately 100 nm. The etch rates for both samples remain constants over time; the as-deposited sample was etched away at a rate of ~3.32 nm/s, which is approximately three times of the etching rate of the crystalline sample, ~1.13 nm/s.

Results

Etch-rate difference between as-deposited and annealed MgCuY thin films. XRD patterns of the as-deposited and annealed MgCuY thin films used in the following experiments were obtained (Fig. 1a). Samples of MgCuY thin films were annealed in a vacuum oven (5×10^{-4} Pa) at a temperature of 573 K for 30 min. The lower blue curve represents the XRD pattern of the as-deposited state, which exhibits no diffraction peaks corresponding to the crystallisation phase. This result indicates that the as-deposited MgCuY thin film, which was prepared via magnetron sputtering, is in an amorphous state. The upper red curve displays the XRD pattern after the annealing. The data show two sharp peaks near the position of 40°, which correspond to the phases of $CuMg_2$ and $MgCu_2$.

The samples used to investigate the etching characteristics were 100-nm-thick MgCuY alloy sputter-deposited onto a 0.8-mm SiO_2 substrate. The etching duration for the amorphous sample was 30 s, while that for the crystalline sample was 70 s. The hollow squares and stars (Fig. 1b) denote the thicknesses of the crystalline and amorphous samples, respectively, after etching for the given duration. Both samples had an approximately constant etch rate over time. For the as-deposited state, the etch-rate function is

$$y = -3.321x + 102.482 \quad (1)$$

For the crystalline state, the etch-rate function is

$$y = -1.131x + 102.734 \quad (2)$$

The etch rate of the as-deposited MgCuY is thus nearly three times of the crystalline film. After 30 s etching, the thickness difference between the crystalline and the as-deposited alloys was nearly 60 nm. We believe that this 3-fold selectivity is unlikely to be the maximum etching selectivity of MgCuY resist, as metallic glasses are strongly composition dependent[32].

Laser-heating simulation for GST and MgCuY alloys. To investigate the disparity between the transient thermal distributions inside the GST and MgCuY thin films, a laser-heating simulation was implemented using the finite element method. In the simulation, two models (Fig. 2a) were constructed using the same geometric dimensions of 20 μm × 20 μm × 4.1 μm, with an alloy thickness of 0.1 μm. The laser beam used to irradiate the models has a Gaussian distribution[33] and an 1-μm radius. The simulated temperature at the edge of the 3D geometry is fixed at 20°C (the ambient temperature), and the models exchange heat with the environment through free convection. The coordinate origin (0, 0, 0) is indicated in the models of Fig. 2a, and all parameters used in the simulation are listed in Table 1.

It is apparent that the green line represents a higher temperature profile than the red line under the same laser irradiation (5 mW, 100 ns); in particular, the central temperature gap (x = 0, z = 0.1 μm) is greater than 400°C (Fig. 2b). However, if the temperatures in the central areas of the two models are the same, the laser power applied to the MgCuY thin film, 224.5 mW, is 44.9 times that applied to the GST thin film. Nevertheless, despite possessing the same central temperature, these two thermal curves are distinct. When the green line (GST, 5 mW) is compared to the blue line (MgCuY, 224.5 mW), it can be seen that the temperature decreases rapidly in the GST thin film from the centre to the edge, whereas in the MgCuY thin film, the temperature decreases more gradually (Fig. 2b).

Six different combinations of laser powers and pulse durations were applied in the simulation to investigate the rate of the temperature decrease from the centre to the edge of the MgCuY thin film (Fig. 2c). The MgCuY thin film was subjected to a laser beam under the following laser-irradiation conditions: a) 50 mW-4 ms, b) 70 mW-6.5 μs, c) 100 mW-290 ns, d) 150 mW-36 ns, e) 250 mW-7 ns and f) 500 mW-1.58 ns. These groups of parameters were selected to maintain a constant temperature at the centre point (0, 0, 0.1 μm). It can be seen that the six curves have the same temperature of approximately 265°C at x = 0 but different rates of temperature decrease from the centre to the edge. The temperature profiles shrink towards the centre from one curve to the next. A higher laser power and shorter pulse duration produce a higher rate of decrease, whereas the temperature profile decreases more gradually in the case of a lower laser power and longer pulse duration. If the crystalline temperature of the MgCuY alloy is assumed to be 200°C, the crystalline area in the case of 500 mW-1.58 ns is a half of that in the case of 50 mW-4 ms. These results imply that the crystalline area in a metallic glass material can be significantly reduced by increasing the laser power while simultaneously decreasing the pulse duration.

The thermal distributions of the two alloys also differ in the longitudinal direction. The laser power used to irradiate the GST thin film is 5 mW, and that used to irradiate the MgCuY film is 80 mW; both have a 400-ns pulse duration. The blue line (Fig. 2d) shows the upper-surface temperature profile in the GST thin film along the x direction, and the red line (Fig. 2d) displays the temperature profile of the bottom surface. There is a clear gap between the two temperature profile curves, and the central temperature gap reaches 450°C.

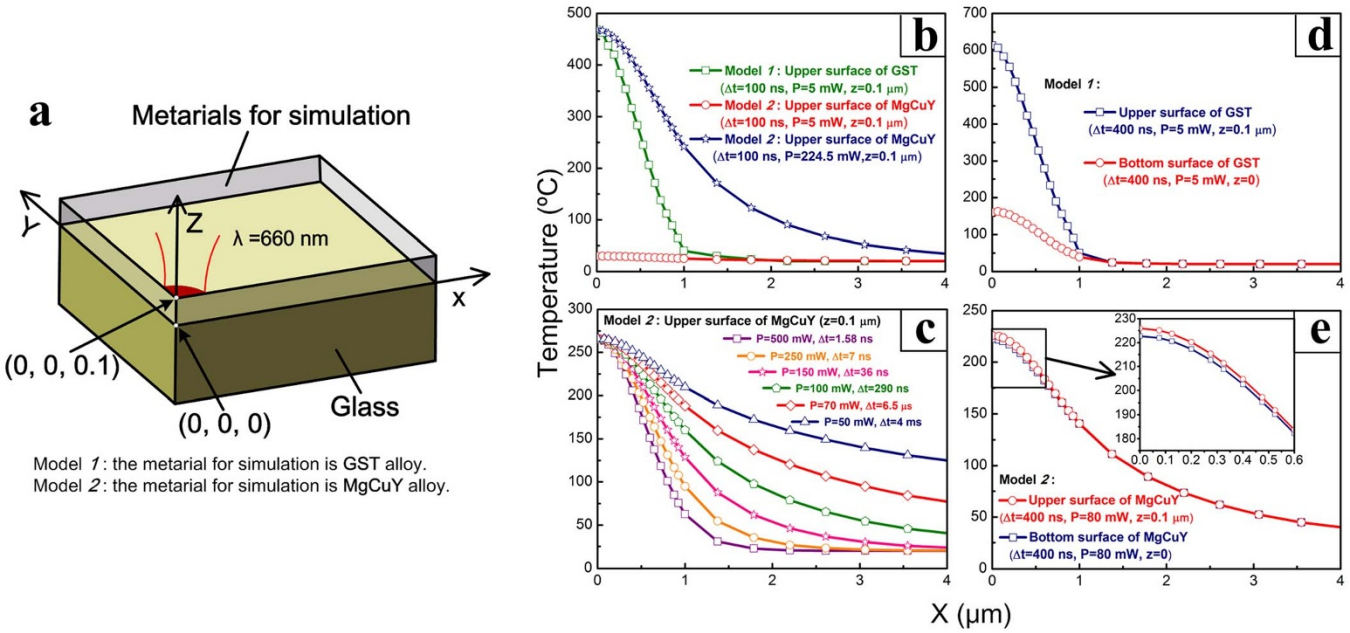

Figure 2 | Computed temperature profiles of GST and MgCuY thin films along the x direction. (a) A schematic of the 3D finite element model of monolayer GST or MgCuY alloy. Both alloy thin films have a thickness of 100 nm, and the glass substrates are 4 μm in thickness. (b) Temperature curves for the upper surfaces of the GST and MgCuY thin films along the x direction. The laser power applied to the GST thin film is 5 mW, whereas those applied to the MgCuY thin film are 5 and 224.5 mW. The duration of the laser pulse is 100 ns. (c) Temperature curves for the upper surface of the MgCuY thin film. The applied laser has a range of laser powers and pulse durations, but different sets of irradiation parameters can lead to the same temperature at the central point. (d) Temperature curves for the upper and bottom surfaces of the GST thin film along the x direction. The laser has a power of 5 mW and a 400-ns duration. (e) Temperature curves for the upper and bottom surfaces of the MgCuY thin film along the x direction. The laser has a power of 80 mW and a 400-ns duration. An enlarged image of the region enclosed by the red square is displayed on the right.

Because of the relatively low thermal conductivity of the GST thin film, it is difficult for the laser-induced heat absorbed by this film to transfer from the top to the bottom, and the temperature profile shrinks inward accordingly. In this case, a crystalline body with the appearance of a bowl should form in the GST thin film. However, the situation in the MgCuY thin film is entirely different from that in the GST film. The red line (Fig. 2e) represents the upper-surface ($z = 0.1$ μm) temperature profile of the MgCuY film along the x direction, and the blue line (Fig. 2e) represents the temperature profile of the bottom surface ($z = 0$) under irradiation conditions of 80 mW and 400 ns. It can be seen that the two lines are nearly coincident; even the enlarged image on the right shows only a small profile gap with a maximum temperature difference of 4°C at $x = 0$. This difference can be ignored in practical applications, and we can regard these two surfaces ($z = 0.1$ μm and $z = 0$) of the MgCuY thin film to have the same temperature profile under the laser irradiation.

Fabricating patterns on MgCuY thin films via laser irradiation and wet etching. A 100-nm-thickness amorphous MgCuY thin film was deposited on a glass substrate and exhibited a relatively smooth cross section surface (Fig. 3a). A continuous-wave laser was used to irradiate the surface of the MgCuY resist to create line patterns. The line patterns on the MgCuY thin films were more easily recognisable under an optical microscope after wet etching (Fig. 3c) in contrast to that before the etching (Fig. 3b). After the MgCuY resist was exposed to the laser, it appeared to shrink slightly inward in the irradiated regions, forming concave shapes (Fig. 3b). However, these concave shapes became convex after the wet-etching process (Fig. 3c).

A discrete dot pattern was also fabricated using a pulse laser. As in the case of the line patterns (Figs. 3a, b), the MgCuY thin film exhibited a higher reflectivity difference between the dots and the amorphous region after the wet-etching process (Figs. 4a, b). Because the amorphous region experiences a higher etching rate compared to the crystalline region (Fig. 1b), bulges were expected to emerge at locations irradiated with a laser pulse. The atomic force micrograph (Fig. 4c) of this sample clearly displays the topography of the generated dot pattern on the MgCuY thin film. The structure of the dot pattern is as predicted above. The average height of the dots is approximately 25 nm (Fig. 4d), and the height difference between two dots is less than 2 nm. As the pulse duration increased from the shortest tested duration, the dot size and height gradually increased, as shown in the cross-sectional profiles (Figs. 4d–g).

Discussion

Copper alloys typically present good corrosion-resistance properties. Crystalline MgCuY thin films primarily consist of $MgCu_2$ and $CuMg_2$ (Fig. 1a), which behave as inert phases, thus leading to a higher etch rate in the amorphous alloy than that in its crystalline counterpart (Fig. 1b). In fact, many metallic glasses exhibit different corrosion resistance or etching selectivity in certain states. Some Fe-based and Cu-based bulk metallic glass (BMG) alloys have been

Table 1 | Parameters applied in the laser-heating simulation[42–45]

Materials	Density (kg/m^3)	Thermal conductivity (w/m K)	Heat capacity (J/kg K)
GST	6150	0.2	210
MgCuY	3130	235	712
SiO_2	2220	1.38	745

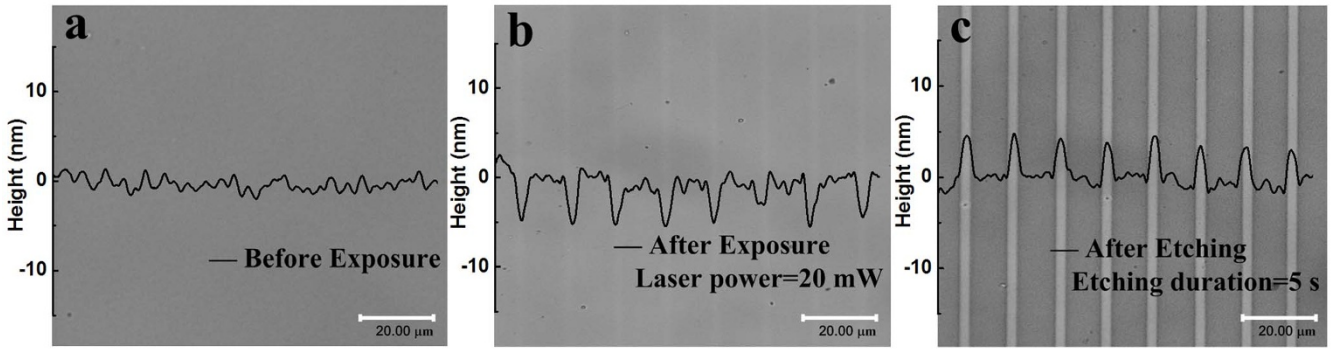

Figure 3 | Continuous line patterns on a MgCuY thin film. (a) An optical micrograph of an amorphous MgCuY thin film deposited on a glass substrate and its cross-sectional profile. (b) The optical micrograph and cross-sectional profile of laser-induced line marks on the MgCuY amorphous thin film after exposure and before wet etching. (c) The optical micrograph and cross-sectional profile of the laser-induced line marks on the MgCuY amorphous thin film after wet etching. The MgCuY thin film was irradiated with a continuous-wave laser and immersed in a 0.5-wt% nitric-acid/ethanol solution for 5 s. The applied laser power was 20 mW. The profile image of the sample was obtained using a surface profiler. The laser wavelength is 660 nm and the N.A. of objective lens is 0.4.

found to exhibit better corrosion properties in the amorphous state than that in the crystalline state[34–36]. In other cases, the corrosion resistance of some Pd-based and Fe-based BMGs amorphous alloys can be improved by annealing[37–39]. Al-based amorphous thin films have also exhibited a lower etching rate after the annealing. These results indicate that both positive and negative resists can theoretically be achieved using metallic glasses for thermal lithography.

The simulation results indicate that the thermal distribution in a MgCuY thin film differs from that in a GST film (Fig. 2). It is apparent that for the same thickness, the heating modes of the two alloys are different. Only the temperature data computed for the alloys ($z = 0$ to $z = 0.1$ μm) are plotted; the temperature in the substrate is ignored (Fig. 5). In images A to F (Fig. 5a), the chromatic regions signify areas in which the temperatures are greater than the crystalline temperature of the GST alloy (approximately 150°C). It can be clearly seen that a bowl-shaped crystalline area forms in the film under laser irradiation, and this area grows as the pulse width increases. In this case, the model of a GST thin film heated by a Gaussian-distributed laser beam can be approximately considered as follows: There exists a point heat source at the coordinates (0, 0, 0.1 μm). The heat-transfer rate in the GST film is assumed to be anisotropic; the transfer rates along the x and y directions are greater than that along the z direction. The arrow in image F indicates the heat-transfer direction in the GST thin film.

The MgCuY alloy has a larger specific heat and a higher thermal conductivity than GST, which indicates that it has a rapid heat-transfer rate. In images A to F (Fig. 5b), the chromatic regions signify areas in which the temperatures are greater than the crystalline temperature of the MgCuY alloy (approximately 200°C). We can see that heat moves rapidly in the vertical direction in the MgCuY thin film, and thus, the temperature profiles on the upper and bottom surfaces become identical within a short time. As the pulse duration increases, the heat moves primarily in a transverse direction from the centre to the edges, as indicated by the arrow in image F. Therefore, the model of a MgCuY thin film heated by a Gaussian beam can be approximately considered as follows: It is assumed that a line heat source exists in the region between (0, 0, 0) and (0, 0, 0.1 μm). This assumed source has the same heat-generation rate at all points along the line, and heat is uniformly transferred from the centre to the edges. The arrow in image F indicates the heat-transfer direction in the MgCuY thin film.

When the above two results are compared, it can be seen that the thermal distribution in the MgCuY thin film is more regular than that in the GST film, and the heat transfer is also better controlled

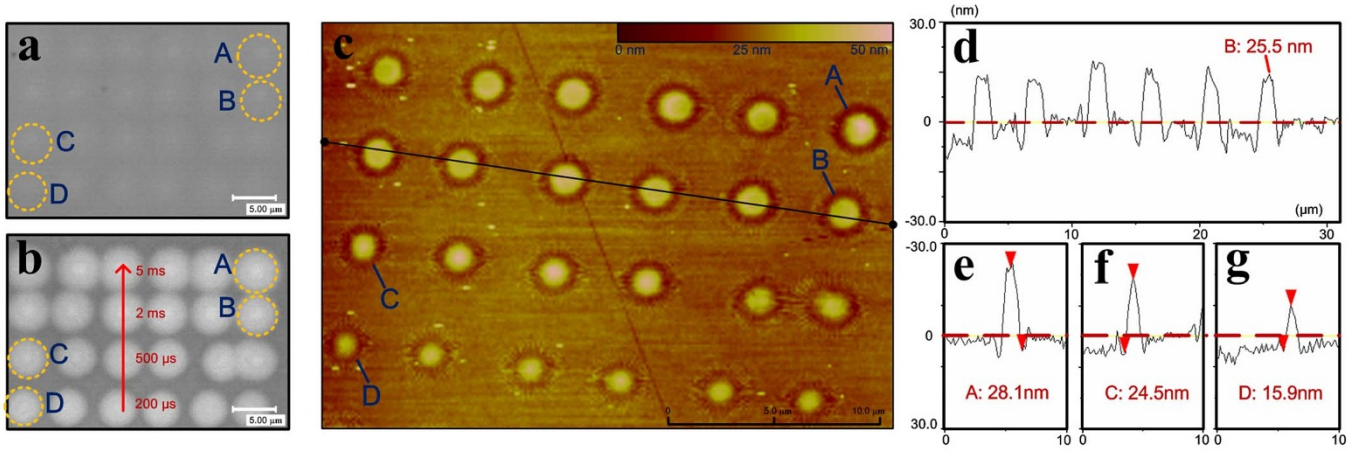

Figure 4 | Discrete dot patterns on a MgCuY thin film. (a) Image of laser-induced marks on an amorphous MgCuY thin film before wet etching under an optical microscope. (b) Marks after wet etching under an optical microscope. (c) An atomic force micrograph (27 μm × 19 μm) of the discrete dot patterns after wet etching. (d) The cross-sectional profile of the second row of the dot array. (e) The cross-sectional profile of bulde **A**. (f) The cross-sectional profile of bulde **C**. (g) The cross-sectional profile of bulde **D**. The laser power in this experiment was 40 mW, and the pulse durations were, from top to bottom, 5 ms, 2 ms, 500 μs, 200 μs. The laser-marked MgCuY sample was subjected to a 5-s etching process in a 0.5-wt% nitric-acid/ethanol solution with a magnetic stirring rate of 300 rpm.

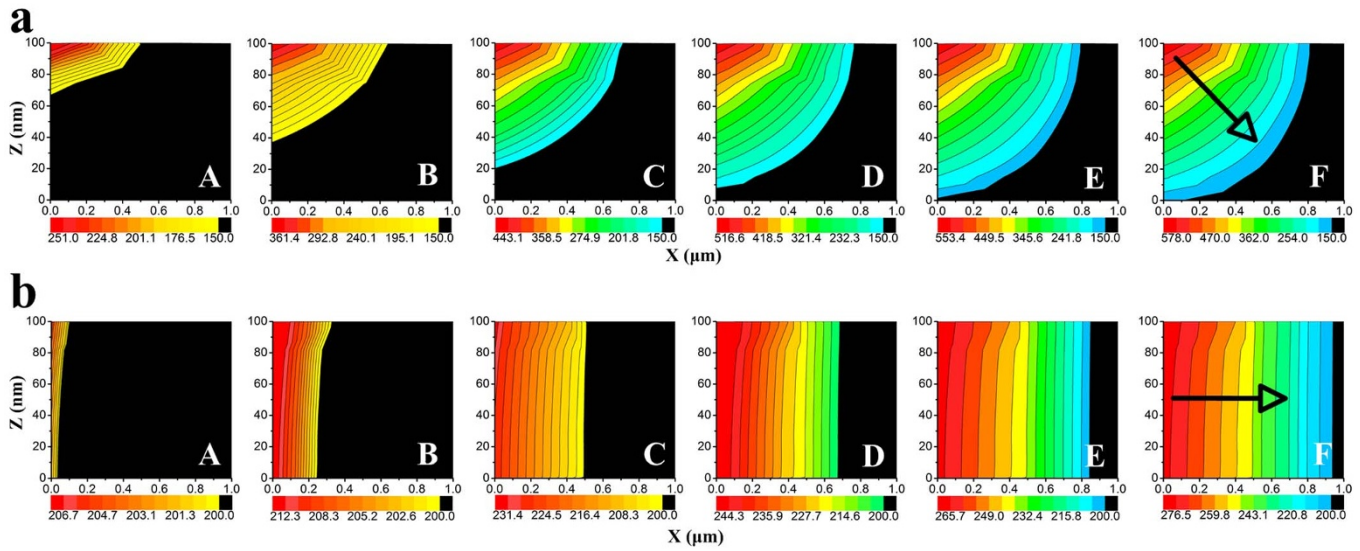

Figure 5 | Images of computed transient thermal contours on an x-z plane cross section in GST and MgCuY. (a) A 5-mW laser beam focused on the surface of a GST thin film for pulse durations of, from A to F, 20, 50, 100, 200, 300 and 400 ns. (b) An 80-mW laser beam focused on the surface of a MgCuY thin film for pulse durations of, from A to F, 200, 300, 500, 1, 2 and 3 μs. For both images, the black regions signify an area in which the temperature is less than the material's crystalline temperature (approximately 150°C for GST and approximately 200°C for MgCuY). Corresponding colour bars are provided on the right-hand side of each contour picture, and the unit is (°C).

because effective heat transmission only occurs in the horizontal direction. The size of the cylindrical crystalline body is directly modulated by the pulse duration when the laser power is a constant, and the pulse direction can be precisely controlled. It should be noted that these results rely on the assumption that the thickness of both alloys is the same as 100 nm. If the thickness of the MgCuY thin film is increased to the micron level or beyond, the heat-transfer mode becomes the same as that in the GST film. The only difference between the two films is that the volume of the bowl-shaped crystalline body in the MgCuY thin film is far greater than that in the GST film because a very high laser power is required to crystallise such a thick metallic glass film. However, for a thickness at the nanometre level, the MgCuY alloy offers distinct advantages with respect to both heat transfer and the crystalline shape, which will be valuable for use as a metallic resist and in other applications.

The fabrication and application steps of a MgCuY thin film resist can be summarised as follows: 1. To coat the MgCuY resist onto the substrate via magnetron sputtering (Figs. 6a, b). It is worth noting that although it is an inorganic resist, the thickness of the MgCuY directly determines the required exposure parameters, as in the case of the organic resists currently applied in optical lithography. The spinning time determines the thickness of a photoresist, whereas the sputtering time determines the thickness of a metallic resist. 2. In accordance with the patterns required, to select an appropriate writing strategy to achieve the laser exposure of the resist (Fig. 6c). The structure of MgCuY changes from "amorphous" to "crystalline" during exposure. The smooth surface becomes concave in the irradiated areas (Figs. 3b, 6c). We consider that this formation of concavities is primarily attributable to the local increase in material density caused by laser-induced crystallisation, which causes the volume of the MgCuY resist to decrease and concavities to be formed. 3. To dip the laser-exposed material into the etchant (0.5 wt% nitric acid/ethanol solution) for a defined duration to form the intended metallic patterns (Fig. 6d). As the wet etching proceeds, the laser-induced concavities rapidly fade away because of the high etching-rate and solubility difference between the amorphous and crystalline regions (Fig. 2b). Raised metallic patterns are fabricated in the irradiated regions following the etching step.

The dimensions (horizontal size and height) of the metallic patterns formed in this manner are proportional to the pulse duration (Figs. 4d–g). This finding indicates that when subjected to a lithography process, the shape of the metallic patterns is not constant but can be modulated by the laser writing strategy. In this way, three-dimensional fabrication[40] should also be possible using metallic resist.

In conclusion, with the development of micro- and nano-fabrication technology, various types of resists have been applied in lithography in the pursuit of better performance. However, the use of metallic materials as a type of resist for lithography has not yet been reported. In this paper, using MgCuY alloy films, we demonstrate that metallic resist is suitable for lithography in principle, and we expect that this type of resist can offer considerable opportunities for

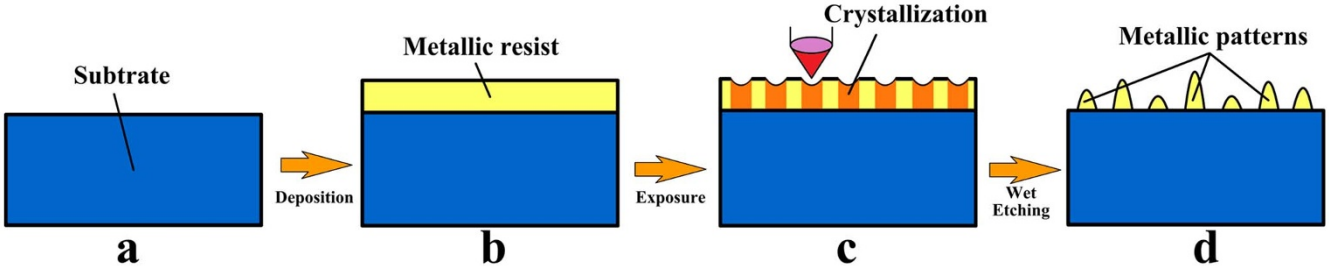

Figure 6 | Schematic diagram of a metallic resist for lithography. (a) Preparation of the substrate. (b) Deposition of the metallic resist onto the substrate. (c) Laser irradiation of the resist. (d) Wet etching to obtain the intended patterns.

development because of its outstanding characteristics. Certainly, MgCuY is not the only feasible type of metallic resist or even necessarily the best one. Other metallic materials may also be suitable for use as resists in lithography. Moreover, the quality (size, height, and side angle etc.) of metallic patterns is affected by many factors, including the thickness of the resist; the laser writing strategy; the material composition; the concentration, temperature and type of etchant applied; the etching time and the rate of magnetic stirring. We believe that as research in this field progresses, metallic resists will achieve outstanding performance in lithography.

Methods

Preparation of MgCuY thin films. MgCuY thin films with a 100-nm height on the substrate were fabricated via optical lithography and magnetron sputtering. A glass wafer was ultrasonically cleaned in water at a temperature of 50°C and then placed on a hot plate to dry. Optical lithography was performed to fill a part of the wafer with photoresist, and magnetron sputtering in conjunction with lift-off was implemented. The MgCuY films that directly adhered to the glass wafer were preserved, whereas those that were deposited on the photoresist were removed by the dissolution of the photoresist. The magnetron-sputtering conditions were as follows: 60 W of DC power, vacuum of 7.8×10^{-5} Pa, 0.5 Pa of Ar^+ pressure and 5 min.

Etching-selectivity experiment. An amorphous thin film of MgCuY was subjected to annealing at 573 K for 30 min in a vacuum oven. Both amorphous and annealed MgCuY thin films were investigated using an X-ray diffraction apparatus (PANalytical Company, Netherlands) to determine whether they were crystalline or amorphous. The XRD test angles ranged from 20° to 70°. A volume of 1.2 ml of 65% nitric-acid solution was slowly added to 500 ml of 98% absolute-ethyl-alcohol solution to obtain a 0.5-wt% nitric-acid/ethanol solution. The solution was stored in a brown bottle and was used as soon as it was mixed. Amorphous and crystalline MgCuY thin films were wet etched using this solution under 300-rpm magnetic stirring for various etching times. After the etching, the samples were soaked in deionised water for 1 min and then blown dry using nitrogen. A surface profiler (KLA-TENCOR Company, USA) was used to determine the height difference between the film and the substrate.

Laser-heating simulation. The finite element method was applied to simulate the laser heating[41]. The model was established as shown in Fig. 2. Considering the spatial symmetry characteristics, only 1/4 of the structure was modelled to reduce the computation time and to permit observations of the thermal distribution in the cross section. The first layer in the model is the MgCuY or GST alloy, and the second layer is the glass wafer. The method of meshing was as follows: **1**. In the first layer, a fine mesh with isometric grids was established within the region of laser irradiation. **2**. Another mesh with non-isometric grids was established in the first layer beyond the region of laser irradiation. The fine level of meshing at the border between the inner and outer regions was the same and decreased inwards and outwards. **3**. A relatively coarse mesh with isometric grids was established throughout the entire second layer (the glass substrate). A heat-flux load with a radius of 1 μm was placed at the centre of the first layer's surface to approximate the laser-heating process. The heat flux has a spatial intensity distribution described by the following equation:

$$\boldsymbol{I}(\boldsymbol{x},\boldsymbol{y}) = \left(1-\boldsymbol{R}_f\right) \times \boldsymbol{P}_0 / \left(\boldsymbol{\pi} \times \boldsymbol{r}_0^2\right) \cdot \exp\left[-\left(\mathbf{x}^2+\mathbf{y}^2\right)/\boldsymbol{r}_0^2\right] \quad (3)$$

Where $\boldsymbol{R}_f$ is the reflectivity of the material, $\boldsymbol{P}_0$ is the laser power and $\boldsymbol{r}_0$ is the 1/e radius. Because the crystalline and melting temperatures of GST and MgCuY alloys are relatively low, heat convection was considered, whereas heat radiation was ignored. Each aspect of the model maintains heat transfer to the surroundings via free convection. The environmental temperature was 20°C, and the free heat-transfer coefficient was 20 W/m^2K. The simulation was performed using ANSYS 13.0 software.

Pattern fabrication. A thermal-lithography optical system was constructed using a semiconductor laser (Coherent Company, USA) connected to, in succession, a laser-beam expander, a polarising beam splitter, a 45° plane mirror and a 0.4-N.A. objective lens. A sample of an MgCuY amorphous thin film was placed on a high-resolution X-Y stepper motor under the objective lens. The laser beam was focused on the sample surface with the aid of an auto-focus system (Sigma KOKI Company, Japan). Crystalline line patterns and dot patterns were created on the MgCuY thin film using a continuous laser and a pulse laser, respectively. The irradiated samples were chemically etched in a nitric-acid/ethanol solution under magnetic stirring. The surface of the MgCuY thin film was oriented away from the direction of the solution flow to prevent the pattern's structure from being affected by the movement of the water. After etching, the sample was soaked in deionised water for 1 min and blown dry using nitrogen. An atomic force microscope (Veeco Company, USA) and a surface profiler were used to characterise the surface morphology of the fabricated patterns.

1. Manfrinato, V. R. *et al.* Resolution limits of electron-beam lithography toward the atomic scale. *Nano. Lett.* **13**, 1555–1558 (2013).
2. Kawata, S., Sun, H. B., Tanaka, T. & Takada, K. Finer features for functional microdevices. *Nature* **412**, 697–698 (2001).
3. Gan, Z. S., Cao, Y. Y., Evans, R. A. & Gu, M. Three-dimensional deep sub-diffraction optical beam lithography with 9 nm feature size. *Nat. Commun.* **4**, 2061 (2013).
4. Abbe, E. Beitrage zur theorie des mikroskops und der mikroskopischen wahrnehmung. Arch. Mikrosk. Anat. Entwichlungsmech. *Arch. Mikrosk. Anat. Entwichlungsmech.* **9**, 413–468 (1873).
5. Levinson, H. J. Overview of Lithography: Challenges and Metrologies. 2003 International Conference: Characterization and Metrology for ULSI Technology, USA. *AIP Conf. Proc.* **683**, 365–370 (2003). http://dx.doi.org/10.1063/1.1622497.
6. Shintani, T., Anzai, Y., Minemura, H., Miyamoto, H. & Ushiyama, J. Nanosize fabrication using etching of phase-change recording films. *Appl. Phys. Lett.* **85**, 639–641 (2004).
7. Lee, Y. C., Chao, S., Huang, C. C. & Cheng, K. C. A compact optical pickup head in blue wavelength with high horizontal stability for laser thermal lithography. *Opt. Express* **21**, 23556–23567 (2013).
8. Deng, C. M., Geng, Y. Y., Wu, Y. Q., Wang, Y. & Wei, J. S. Adhesion effect of interface layers on pattern fabrication with GeSbTe as laser thermal lithography film. *Microelectron. Eng.* **103**, 7–11 (2013).
9. Chu, C. H. *et al.* Laser-induced phase transitions of $Ge_2Sb_2Te_5$ thin films used in optical and electronic data storage and in thermal lithography. *Opt. Express.* **18**, 18383–18393 (2010).
10. Khaleque, T., Svavarsson, H. G. & Magnusson, R. Fabrication of phase-change chalcogenide $Ge_2Sb_2Te_5$ patterns by laser-induced forward transfer. *Opt. Express.* **19**, 16975–16984 (2011).
11. Deng, C. M., Geng, Y. Y. & Wu, Y. Q. New calix[4]arene derivatives as maskless and development-free laser thermal lithography materials for fabricating micro/nano-patterns. *J. Mater. Chem. C.* **1**, 2470–2476 (2013).
12. Kim, J. H., Lim, J. & Lee, J. S. Wet-etching characteristics of GeSbTe phase-change films for high density media. Optical Data Storage 2007, USA. *Proc. SPIE.* **6620**, 66202D–66202D6 (2007). doi:10.1117/12.755470.
13. Lin, Y. *et al.* Ultrafast-laser induced parallel phase-change nanolithography. *Appl. Phys. Lett.* **89**, 0411081–0411083 (2006).
14. Liu, C. P., Hsu, C. C., Jeng, T. R. & Chen, J. P. Enhancing nanoscale patterning on Ge-Sb-Sn-O inorganic resist film by introducing oxygen during blue laser-induced thermal lithography. *J. Alloy. Compd.* **488**, 190–194 (2009).
15. Kuwahara, M. *et al.* Thermal lithography for 0.1 μm pattern fabrication. *Microelectron. Eng.* **61–62**, 415–421 (2002).
16. Kuwahara, M., Kim, J. H. & Tominaga, J. Dot formation with 170-nm dimensions using a thermal lithography technique. *Microelectron. Eng.* **67–68**, 651–656 (2003).
17. Lin, Y. *et al.* Hybrid laser micro/nanofabrication of phase change materials with combination of chemical processing. *J. Mater. Process. Tech.* **192**, 340–345 (2007).
18. Lin, Y. *et al.* Patterning of phase change films with microlens arrays. *J. Alloys. Compd.* **449**, 253–257 (2008).
19. Chong, T. C., Hong, M. H. & Shi, L. P. Laser precision engineering: from microfabrication to nanoprocessing. *Laser. Photonics. Rev.* **4**, 123–143 (2010).
20. Oak, J. J. *et al.* Investigation of glass-forming ability, deformation and corrosion behavior of Ni-free Ti-based BMG alloys designed for application as dental implants. *Mat. Sci. Eng. C-Bio S.* **29**, 322–327 (2009).
21. Jang, D. C. & Greer, R. J. Transition from a strong-yet-brittle to a stronger-and-ductile state by size reduction of metallic glasses. *Nat. Mater.* **9**, 215–219 (2010).
22. Ye, J. C., Lu, C., Liu, C. T., Wang, Q. & Yang, Y. Atomistic free-volume zones and inelastic deformation of metallic glasses. *Nat. Mater.* **9**, 609–612 (2010).
23. Tian, L. *et al.* Approaching the ideal elastic limit of metallic glasses. *Nat. Commun.* **3**, 609–614 (2012).
24. Gu, X. N. *et al.* Corrosion of, and cellular responses to Mg–Zn–Ca bulk metallic glasses. *Biomaterials.* **31**, 1093–1103 (2010).
25. Mei, J. N. *et al.* Formation of Ti–Zr–Ni–Cu–Be–Nb bulk metallic glasses. *J. Alloy. Compd.* **467**, 235–240 (2009).
26. Huang, J. C., Chub, J. P. & Jang, J. S. C. Recent progress in metallic glasses in Taiwan. *Intermetallics* **17**, 973–987 (2009).
27. Lee, M. L. *et al.* High-resolution mastering using AlNiGd metallic glass thin film as thermal absorption layer. *Intermetallics* **18**, 2308–2311 (2010).
28. Kumar, G., Tang, H. X. & Schroers, J. Nanomoulding with amorphous metals. *Nature* **457**, 868–872 (2009).
29. Radha, B., Lim, S. H., Saifullah, M. S. M. & Kulkarni, G. U. Metal hierarchical patterning by direct nanoimprint lithography. *Sci. Rep.* **3**, 1078 (2013).
30. Hirata, A. *et al.* Geometric Frustration of Icosahedron in Metallic Glasses. *Science* **341**, 376–379 (2013).
31. Cheng, Y. Q. & Ma, E. Atomic-level structure and structure–property relationship in metallic glasses. *Prog. Mater. Sci.* **56**, 379–473 (2013).
32. Mezbahul-Islam, M. & Medraj, M. Phase equilibrium in Mg-Cu-Y. *Sci. Rep.* **3**, 3033 (2013).
33. Mansuripur, M., Neville, G. A. & Goodman, J. W. Laser-induced local heating of multilayers. *Appl. Optics.* **21**, 1106–1114 (1982).
34. Wu, Y. F., Chiang, W. C. & Wu, J. K. Effect of crystallization on corrosion behavior of $F_{40}Ni_{38}B_{18}Mo_4$ amorphous alloy in 3.5% NaCl solution. *Mater. Lett.* **62**, 1554–1556 (2008).
35. Chiang, W. C., Yeh, W. D. & Wu, J. K. Hydrogen permeation in $Fe_{40}Ni_{38}B_{18}Mo_4$ and $Fe_{81}B_{13.5}Si_{3.5}C_2$ amorphous alloys. *Mater. Lett.* **59**, 2542–2545 (2005).

36. Lin, H. M., Wu, J. K., Wang, C. C. & Lee, P. Y. The corrosion behavior of mechanically alloyed Cu–Zr–Ti bulk metallic glasses. *Mater. Lett.* **62**, 2995–2998 (2008).
37. Wu, Y. F., Chiang, W. C., Chu, J. P., Nieh, T. G. & Kawamura, Y. W. Corrosion resistance of amorphous and crystalline $Pd_{40}Ni_{40}P_{20}$ alloys in aqueous solutions. *Mater. Lett.* **60**, 2416–2418 (2006).
38. Szewieczek, D., Held, J. T. & Paszenda, Z. Corrosion investigations of nanocrystalline iron based alloy. *J. Mater. Process. Technol.* **78**, 171–176 (1998).
39. Thorpe, S. J., Ramaswami, B. & Aust, K. T. Corrosion and auger studies of a nickel-base metal-metalloid glass. *J. Electrochem. Soc.* **135**, 2162–2170 (1988).
40. Lin, Y. *et al*. Three Dimensional Micro/Nano-structure Fabrication of Phase-change Film. *J. Laser. Micro. Nanoen.* **3**, 52–57 (2008).
41. Liu, F. R. *et al*. An explanation of the crystallization of amorphous $Ge_2Sb_2Te_5$ films induced by a short Gaussian laser pulse. *Appl. Phys. Lett.* **103**, 051905 (2013).
42. Long, X. M. *et al*. Dynamic switching characteristic dependence on sidewall angle for phase change memory. *Solid. State. Electron.* **67**, 1–5 (2012).
43. Pryds, N. H. *et al*. Preparation and Properties of Mg-Cu-Y-Al Bulk Amorphous Alloys. *Mater. Trans.* **41**, 1435–1442 (2000).
44. Petersen, K. E. Dynamic micromechanics on silicon: techniques and devices. *Ieee. T. Electron. Dev.* **25**, 1241–1250 (1978).
45. Incropera, F. P. & DeWitt, D. P. [Thermophysical Properties of Matter] *Fundamentals of Heat and Mass Transfer* [Ratts, L. (ed.)] [988] (John Wiley & Sons, New York, 2011).

Acknowledgments

We sincerely thank Dr. Zhe Guo for his assistance with the cross-section profiler measurement. This work was supported by grants from the Ph.D. Programs Foundation of the Ministry of Education of China (No.90142110003), National High-tech R&D Program of China (863 Program, No. 2014AA032903) and National Natural Science Foundation of China (No. 61306005, 61376130).

Author contributions

B.J.Z., Z.L. and X.S.M. designed the experiments. B.J.Z. designed and constructed the optical system for thermal lithography. B.J.Z. and J.Z.H. conducted the lithography experiments. B.J.Z. and R.W.N. performed the simulations and analysed data. N.N.Y., W.W. and Y.Z.H. deposited the materials for the experiments. B.J.Z. drafted the paper. All authors discussed the results and commented on the manuscript. X.S.M. directed the project and provided overall guidance.

Additional information

Competing financial interests: The authors declare no competing financial interests.

How to cite this article: Zeng, B.J. *et al*. Metallic resist for phase-change lithography. *Sci. Rep.* **4**, 5300; DOI:10.1038/srep05300 (2014).